Ripple and Lotus Phenomenon: Radiation Pattern Evolution of Nonlinear Thomson Scattering Under Cooperative and Competitive Effects of Applied Magnetic and Laser Field

Yi Zhang , Feiyang Gu , Haokai Wang, Qingyu Yang , Yubo Wang, Xingyu Li , and Youwei Tian

Abstract—This paper focuses on the scenario where relativistic electron nonlinear Thomson forward scattering is driven by circularly polarized laser pulses, using both theoretical analysis and numerical simulations. For the first time, we investigate how the magnetic flux density and beam waist radius jointly influence the spatiotemporal properties of radiation. For the superimposed field under different parameters, the forces exerted by the laser field and the applied magnetic field on electrons will show cooperative or competitive relationships at different moments of action. And the transformation of this relationship promotes the evolution of the electron radiation pattern in the superimposed field, which greatly changes the spatiotemporal properties of Thomson scattering. Based on this, completely new spatial distributions of radiation-ripple and lotus phenomena were discovered. In addition, the combination of parameters with the best radiation properties was selected through Big Data, and the quasi-periodicity of the azimuth angle ϕ_p was discovered for the first time. These results will contribute to the understanding of the radiation mechanism of Thomson scattering in superimposed field and will be instructive for laboratory modulation of ultra-high-performance X/γ-rays.

Index Terms—Laser-matter interaction, nonlinear thomson scattering, radiation pattern evolution, ripple and lotus phenomenon, ultrafast optics and nonlinear effects.

I. INTRODUCTION

THE field of interactions of ultrashort, ultra-intense lasers with matter has been of wide interest to physicists over the past few decades [1], [2]. With the successive advent of mode-locked lasers [3], [4], fiber lasers [5], [6] and chirped pulse amplification (CPA) [7], [8], [9] laser pulses with intensity up

to 10^{23} W/cm^2 have further advanced the field of ultrafast laser physics [10]. And nonlinear Thomson scattering has become a hot research direction in this field due to its great application prospects as a radiation source of high-energy ultrashort X-rays and γ-rays [11], [12], [13]. It has a very wide range of applications in the fields of biomedicine [14], [15], astrophysics [16], [17], and laser detection [18], [19].

Thomson scattering is a scattering process of relativistic charged particles in a strong electromagnetic field, and the Doppler effect is the underlying cause of its remarkable nonlinearity. In the past works, Zhang et al. [20] and Yan et al. [21] investigated the effects of pulse width and initial position of electrons on the peak radiated power and spatial properties of Thomson scattering, respectively. However, the improvement of the radiated power is very limited, so Yang et al. [11] proposed to obtain ultra-intense X-rays by nonlinear inverse Thomson scattering (NITS) of off-axis electrons with intense laser pulses. Xie et al. [22] and Faisal et al. [23] investigated the electrodynamic properties of nonlinear Thomson scattering and the spatial properties of forward radiation spectra after the introduction of a constant background magnetic field into the laser field, respectively. While Xie et al. [24] and Hong et al. [25] studied Thomson backscattering in a superimposed field, they theoretically realized the modulation of THz radiation in this way. Nishiura et al. [26] studied the collective Thomson scattering of an incident X-mode wave in magnetized electron and positron pair plasma under a strong magnetic field, providing an important theoretical foundation for understanding radiation behavior in strongly magnetized plasma. Mushtukov et al. [27], [28] studied the Compton scattering of polarized radiation and the statistical properties of multiple Compton scatterings in a strong magnetic field, which represents the extreme case of nonlinear Thomson scattering. Based on the above research, this paper proposes for the first time that the radiation properties of nonlinear Thomson forward scattering (NTFS) can be greatly improved by introducing an applied magnetic field.

Under the framework of classical electrodynamics, this paper studies the spatiotemporal properties of NTFS pulses when circularly polarized laser pulses drive initially stationary electrons to move relativistically under an applied magnetic field through numerical simulation, as shown in Fig. 1. Based on special
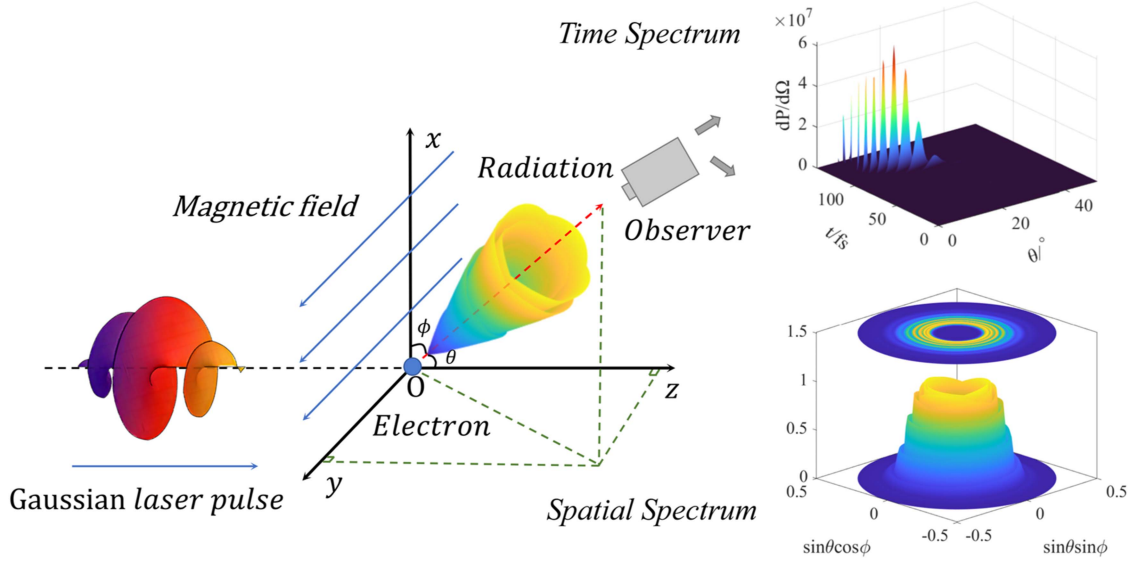
Fig. 1. Schematic of nonlinear Thomson forward scattering of a stationary electron in a circularly polarized Gaussian laser field with an applied magnetic field.

relativity and Lienard-Wiechert potentials, the coupling effects of the pair of cross-parameters, magnetic flux density (radial distribution of the magnetic field) and beam waist radius (longitudinal distribution of the laser field), on the spatiotemporal properties are investigated in detail in all directions. We classify three types of radiation patterns based on the spatiotemporal properties of NTFS. And then the evolution of the radiation pattern as the parameters are varied is analyzed in terms of the competition and cooperation between the laser field and the applied magnetic field. Interestingly, we found a new spatial distribution of radiation - ripple radiation, which is different from the radiation pattern whose spatial distribution of radiation is annular or vortex [29]. The ripple phenomenon not only has irreplaceable advantages in practical applications due to its unique spatial distribution, but also serves as a transitional phenomenon, marking the boundary between different radiation patterns. In addition, we selected a combination of NTFS parameters with ultra-high power, good directivity and high collimation based on ultra-large-scale numerical simulations.

II. THEORY AND FORMULATION

First of all, it should be noted that for all formulas and definitions in this paper, the time and space coordinates are normalized by $\omega_0^{-1} = \lambda_0/2\pi c$ (the reciprocal of the laser circular frequency) and $k_0^{-1} = \lambda_0/2\pi$ (the reciprocal of the wave number in the laser vacuum), respectively. $\lambda_0 = 1\mu m$ is the wavelength of the laser in this paper. c is the speed of light in vacuum.

The schematic of the NTFS model is shown in Fig. 1. Based on this model, we introduced a stationary single electron at the origin and a circularly polarized Gaussian laser pulse along the $+z$-axis with an incident angle $\sigma_{in} = 0$ at the $-z$-axis. At the same time, to the laser field, we add a non-uniform magnetic field pointing in the y direction with a magnetic field strength proportional to x.

By solving the paraxial approximate solution of the Helmholtz equation, we can describe the total vector potential $\boldsymbol{a}$ of the above superimposed field as [22], [25]:

$$\boldsymbol{a} = \boldsymbol{A}(\eta) + \boldsymbol{B}(x)$$

$$\boldsymbol{A}(\eta) = a_l \left[\cos(\varphi)\vec{\mathbf{x}} + \delta\sin(\varphi)\vec{\mathbf{y}}\right]$$

$$\boldsymbol{B}(x) = B_0\, x\vec{\mathbf{y}} \tag{1}$$

where $\boldsymbol{A}(\eta)$ is a circularly polarized Gaussian laser pulse and $\boldsymbol{B}(x)$ is an applied magnetic field. $a_l = a_0 \exp(-\eta^2/L^2)\exp(-\rho^2/b^2)(b_0/b)$ and a_0 is the peak amplitude of the laser normalized by mc^2/e. $\eta = z - t$ is a phase factor that reveals the variation of the electromagnetic wave in time and space. L is the pulse width of the laser pulse. $\rho = (x^2 + y^2)^{1/2}$, represents the off-axis distance of the electron. b_0 is the beam waist radius of the laser, i.e., the cross-section radius of the narrowest part of the Gaussian beam (the beam waist is at $z = 0$ in this paper), and the beam at the beam waist is the most concentrated and has the highest intensity. $b = b_0(1 + z^2/z_f^2)^{1/2}$ is the radius of the beam when the laser propagates to z, where $z_f = b_0^2/2$ is the Rayleigh distance of the laser. δ is the polarization parameter of the laser, and in this paper $\delta = 1$ corresponds to a circularly polarized laser pulse. The total phase of the laser can be expressed as:

$$\varphi = \eta + \varphi_R - \varphi_G + \varphi_0 \tag{2}$$

where $\varphi_R = \rho^2/2R(z)$, $R(z) = z(1 + z_f^2/z^2)$ is the radius of curvature of the wavefront. $\varphi_G = tan^{-1}(z/z_f)$ is the Gouy phase, which represents the additional nonlinear additive phase shift produced by the laser as it passes through its beam waist. $\varphi_0 = 0$ is the initial phase of the laser, which represents the phase when the electrons and the laser first interact. B_0 is the magnetic flux density of the applied magnetic field. The two terms of (1) represent the laser field component and the magnetic field component of the superimposed field, respectively. Where

$\exp(-\eta^2/L^2)(b_0/b)$ in the first term corresponds to the longitudinal Gaussian distribution of the Gaussian laser pulse, while $\exp(-\rho^2/b^2)$ corresponds to the radial Gaussian distribution.

In the rectangular coordinate system, based on the Coulomb gauge of the laser field $\nabla \cdot \boldsymbol{A} = 0$, the normalized vector potential $\boldsymbol{a}$ of the superimposed field can be further decomposed into radial and longitudinal fields:

$$a_x = a_l \cos(\varphi)$$
$$a_y = a_l \sin(\varphi) + B_0 x$$
$$a_Z = 2a_l[-x\sin(\varphi+\theta) + \delta y \cos(\varphi+\theta)]/b_0 b \quad (3)$$

where $\theta = \pi - tan^{-1}(z/z_f)$. We find that the introduction of an applied magnetic field changes the y-axis component of the total vector potential $\boldsymbol{a}$, which in turn affects the electron trajectory and the radiation properties of the electron. This is also the reason why $\boldsymbol{a}$ does not satisfy the Coulomb gauge. Based on the above equations and the Hamiltonian description, the equation of motion of a single electron in an electromagnetic field can be described by the Lorentz equation and the energy equation of the electron [11], [30]:

$$\partial_t(\boldsymbol{p} - \boldsymbol{a}) = -\nabla_a(\boldsymbol{u} \cdot \boldsymbol{a})$$
$$d_t\gamma = \boldsymbol{u} \cdot \partial_t\boldsymbol{a} \quad (4)$$

where $\boldsymbol{u}$ is the electron velocity normalized by the speed of light c, $\boldsymbol{p} = \gamma\boldsymbol{u}$ is the electron momentum normalized by mc, and $\gamma = (1 - \boldsymbol{u}^2)^{-1/2}$ is the Lorentz factor. where $c = 2.998 \times 10^8 m/s$ and the mass of the electron $m = 9.109 \times 10^{-31}$ kg. The subscript a in ∇_a indicates that ∇ acts on $\boldsymbol{a}$ only. By substituting (3) into (4), the partial differential equation is solved through the 8-9 order Runge-Kutta algorithm to obtain the trajectory equation and the motion state of the electron in all space and time. At the same time, we introduced GPU parallel solving based on CPU serial. Based on the serial-parallel combination, adaptive and automated programming is carried out, thereby obtaining a large amount of ultra-high-precision data.

In the spherical coordinate system, based on the motion state of the electron at each time step, the radiated power per unit solid angle can be derived from the Poynting vector of the relativistic moving electron:

$$P(t)_\Omega = \frac{dP(t)}{d\Omega} = \left[\frac{|\boldsymbol{n}| \times [(|\boldsymbol{n}| - \boldsymbol{u}) \times d_t|\boldsymbol{u}|^2}{(1 - \boldsymbol{n} \cdot \boldsymbol{u})^6}\right]_{t'} \quad (5)$$

$P(t)_\Omega$ is normalized by $e^2\omega^2/4\pi c$. In the formula, the radiation direction $\boldsymbol{n} = \sin(\theta)\cos(\varphi) \cdot \tilde{\mathbf{x}} + \sin(\theta)\sin(\varphi) \cdot \tilde{\mathbf{y}} + \cos(\theta) \cdot \tilde{\mathbf{z}}$, is a unit vector in the spherical coordinate system. θ and φ represent the polar angle and azimuthal angle respectively, as shown in Fig. 1. $d\Omega$ represents the solid angle on the unit sphere. $d_t\boldsymbol{u}$ represents the acceleration of electrons. The subscript $t' = t - R_0 + \boldsymbol{n} \cdot \boldsymbol{r}$, denotes the moment when the laser interacts with the electrons, while t denotes the moment when the radiation is observed at the observation point. R_0 and $\boldsymbol{r}$ denote the distance from the origin to the observation point and the position vector of the electron, respectively. In this paper, the

NTFS is observed on a sphere centered at the coordinate origin with a radius of $1m$, i.e., $R_0 = 1m$.

III. NUMERICAL RESULTS

In this paper, the wavelength of the incident circularly polarized laser pulse $\lambda_0 = 1\mu m$, and the normalized light intensity parameter $a_0 = 5$ (corresponding to the peak laser intensity $I_L = 3.45 \times 10^{19}$ W/cm^2). The pulse width $L = 5\lambda_0$ and the initial position of the pulse center at $(0, 0, -6L)$. The beam waist radius $b_0 = 2 \sim 20\lambda_0$, the initial phase $\varphi_0 = 0$. The magnetic flux density of the applied magnetic field $B_0 = 0 \sim 0.5$. The initial energy of the electron $\gamma_0 = 1$. In the following section, we reveal the evolution of the radiation pattern and find the boundary phenomenon for pattern determination by studying the full-angle radiation characteristics, electron trajectories, and three-dimensional time spectrum of NTFS in the superimposed field.

A. Electron Trajectories and Radiated Power Curves

In Fig. 2 we investigate the coupling effect of the crossover parameter on the electron trajectory and the radiated power throughout the process. One dimension is a gradual increase in magnetic flux density from left to right, i.e., the radial influence of the magnetic field is increasing. The other dimension is the increasing beam waist radius from top to bottom, i.e., the slowing down of the longitudinal strength decay of the laser field. The laser field interacts more fully with the electrons, which we can interpret as an increased effect of the laser field. The two compete for the dominant factor in NTFS. We divide the superimposed field into three parts based on the strength relationship between the two in terms of their determinism of the electron radiation pattern. That is, the superimposed field dominated by the applied magnetic field (CDM), the superimposed field dominated by the laser field (CDL), and the superimposed field in which the laser and magnetic fields are evenly matched (CDLM). Corresponding to the upper triangle, lower triangle and the transition area framed by the black ladder in Fig. 2 respectively. Note that for the column with a magnetic flux density $B_0 = 0$, it does not participate in the above division since it is only influenced by the laser field.

In Fig. 3, we examine the trajectory properties of electrons during relativistic motion in a superimposed field. Together with Fig. 2, these figures show the electrodynamic properties of the electron. Interestingly, Figs. 3 and 8 have exactly the same division of the regions, and both are divided by cliff-like mutations. This indicates that both the electrodynamic properties of the electron and the radiation properties of nonlinear Thomson scattering satisfy to the division into CDM, CDLM and CDL regions, and any of these parameters can be used to quickly determine the current radiation pattern of the electron.

Since the calculation of the motion parameters of the electron is less than one ten-thousandth of the radiation properties, it can be used as an important basis for quickly determining the radiation pattern. More importantly, Fig. 3(b) is almost identical to Fig. 8(a), which indicates that the maximum energy $\gamma_{\max}$ of the electron and the maximum radiated power $P_{\Omega\max}$ maintain
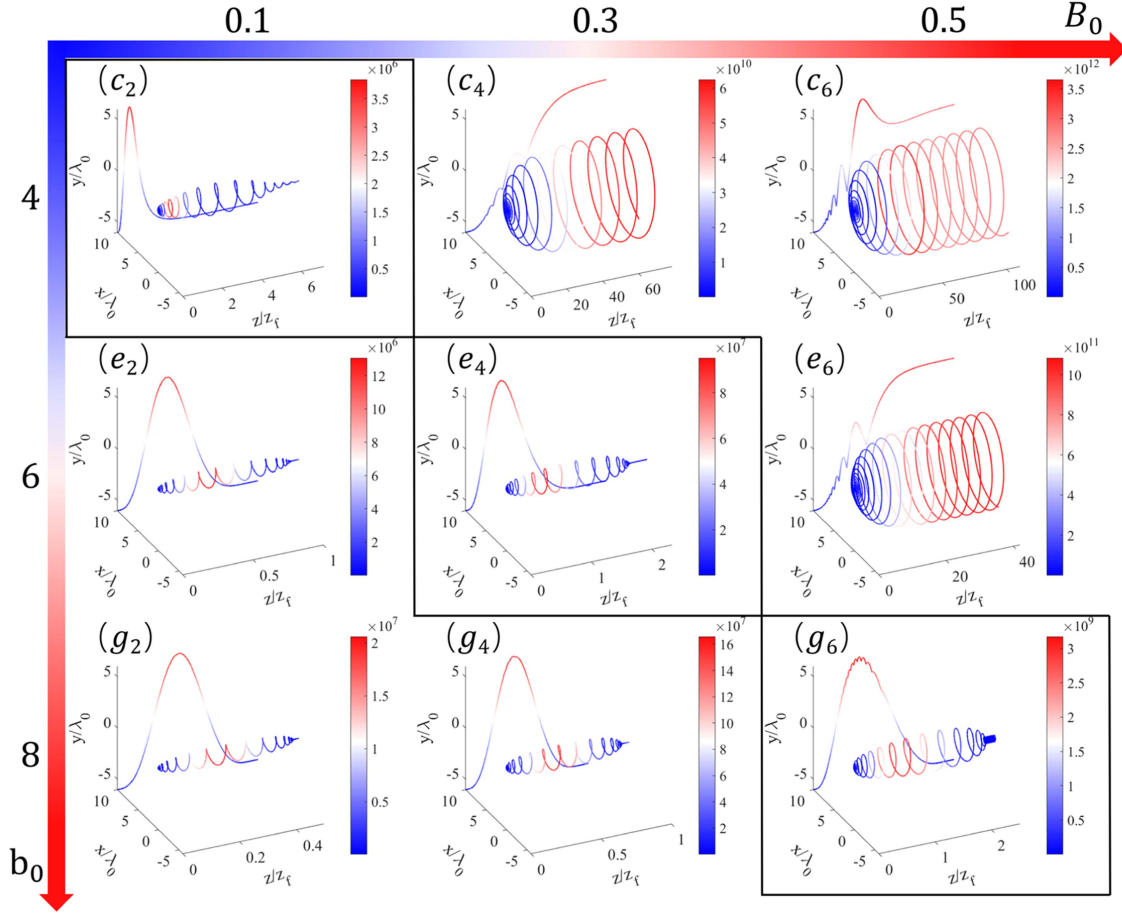
Fig. 2. Trajectories of electrons in the superimposed field and their radiated power at their corresponding positions, where the color scale of each plot is separately normalized by its own maximum radiated power. Figure matrix compares different magnetic flux densities B_0 horizontally, and different beam waist radius b_0 vertically. The black curves in the figure divide the radiation patterns of the NTFS, i.e., the different regions of the superimposed field (see Visualization 1).
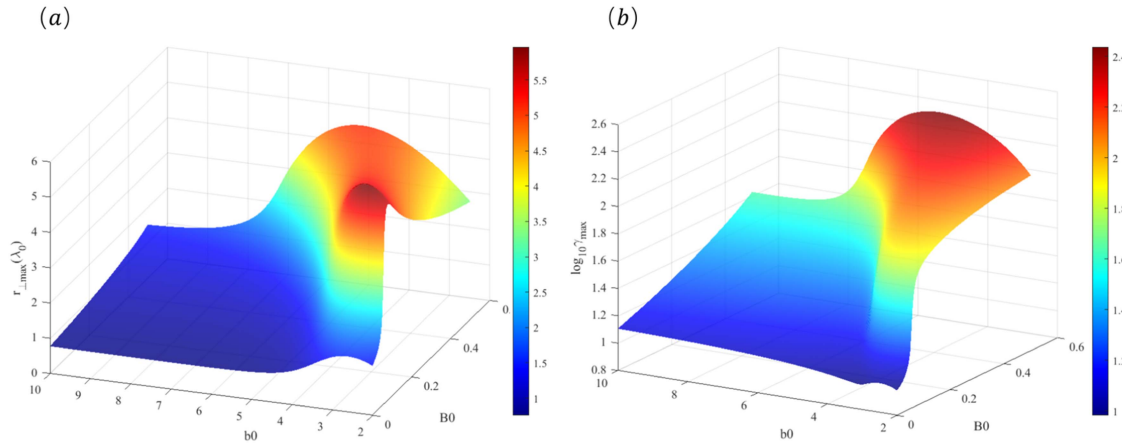

Fig. 3. Under different magnetic flux density B_0 and different beam waist radius b_0, the maximum orbiting radius $r_{\perp\max}$ of electrons when NTFS (a), the maximum energy of electrons $\log_{10}\gamma_{\max}$ (b).

the sameness when the parameter changes. It is instructive for rough estimation of $P_{\Omega\max}$. However, in the CDM region, the distributions of Fig. 3(a) and (b) are not exactly the same. $r_{\perp\max}$ in Fig. 3(a) is not positively correlated with B_0, but shows a saddle surface, with a valley at $B_0 = 0.4$.

Considering that this paper introduces a non-uniform magnetic field in relativistic electrodynamics, the forces on electrons in it are totally different from the uniform magnetic field. The electromagnetic tensor, four-dimensional Lorentz force, magnetic gradient force, etc. need to be considered in the actual

numerical simulation. To simplify the analysis process, we decompose the Lorentz force orthogonally into a radial Lorentz force $f_\perp$ and a longitudinal Lorentz force f_z to explain the relevant mechanism.

Once the electrons start to move, the $f_\perp$ of the applied magnetic field on the electrons always points in the off-axis direction, causing the orbiting radius $r_\perp$ to tend to become larger. Therefore, the radial work $W_{M\perp}$ of the magnetic field is constantly positive. Although f_z keeps oscillating between pointing to $-z$ and $+z$, considering an oscillation period, the longitudinal work of the magnetic field $W_{M\perp}$ and the change in the electron's own energy ΔE_E satisfy $sgn(W_{Mz}) = sgn(\Delta E_E)$. The work done by the magnetic field [31], [32] on the electrons $W_M = W_{M\perp} + W_{Mz}$. According to the energy conservation theorem:

$$W_L + W_M + W_R = \Delta E_E \tag{6}$$

Where W_L and W_R are the work done on the electron by the laser field and the energy lost by the electron due to radiation, respectively. Differentiate (6) for time:

$$P_L + P_M + P_R = \Delta P_E \tag{7}$$

The above equation is the instantaneous power conservation equation obtained by taking a single electron as a system. Where P_L and P_M are the instantaneous power of the work done on the electron by the laser field and the applied magnetic field, respectively. $|P_L| \propto |\partial a_l/\partial \eta|$, $P_{M\perp} \propto u_z$ and $P_{M\perp} \propto r_\perp$. P_R is the instantaneous radiated power of the electron, while ΔP_E on the right side of the equation corresponds to the instantaneous amount of change in the electron's own energy. At the rising edge of the laser, the laser drives the electrons in a helical motion with increasing pitch. Both P_L and P_M are positive, and the laser field and the applied magnetic field are in a cooperative relationship. At this time, most of the energy gained by the electrons in the superimposed field is converted into ΔE_E, and only a small part is radiated as W_R. At the falling edge, the relationship between the two fields in different partitions is very different, according to which three radiation patterns are differentiated.

In the CDL region, since the applied magnetic field is weaker relative to the laser field, P_R decreases sharply as soon as the laser enters the falling edge ($P_L < 0$), and ΔP_E also decreases with the decreasing electron velocity. This is corroborated by the Gaussian distribution of the radiated power curves in the CDL region in Fig. 2. It shows that the radiated power P_R appears at the maximum value $P_{R\max}$ near the intersection of the rising edge and the falling edge of the laser pulse, which is recorded as the peak radiated power. At this point, although $P_{M\perp} > 0$, $P_M = P_{M\perp} + P_{Mz} < 0$, the magnetic field also does negative work on the electrons, and the laser and magnetic fields are still cooperating. The electron trajectories in the CDL region in Fig. 2. are extremely similar to those in the pure laser field. On the one hand, it exhibits a quadratic symmetry about the z-axis. On the other hand, it is symmetric about the left-right symmetry of the cross section perpendicular to the z-axis at the maximum orbiting radius $r_{\perp\max}$. The circularly polarized property of the laser field and the approximate symmetry of the rising and falling edges of the non-tightly focused laser

pulse are reflected, respectively. Since the laser field in the CDL region plays a major role in the NTFS of electrons and the radiation properties are extremely similar to those of the pure laser field, we attribute the radiation pattern in the CDL region to the laser field radiation. Fixing the beam waist radius and gradually enhancing the magnetic field, the peak radiation point is gradually shifted from the rising edge to the falling edge of the Gaussian laser pulse. It can be found that the maximum longitudinal displacement d_{zmax}, and $P_{R\max}$ are all increasing synchronously, and slight oscillations begin to appear at the peak of the power curve.

The relationship of the superimposed field in the CDM region is diametrically opposed. After the electrons start to interact with the falling edge of the laser, even though the laser field does negative work trying to decelerate the electrons, the strong magnetic field provides $f_\perp \gg 0$ making $P_{M\perp} > P_L + P_R$. The electrons continue to accelerate, P_R and $r_\perp$ continue to increase and $\Delta P_E > 0$. As the center of the laser pulse moves away from the electrons, the longitudinal component $\exp(-\eta^2/L^2) \approx 0$, and thus $P_L \approx 0$. At the same time, the speed of the electrons is extremely close to the speed of light, so that the energy of the electrons is saturated and $\Delta P_E \approx 0$. Therefore, $P_M = -P_R$, meaning all the energy that the electrons gain from the magnetic field is radiated out as electromagnetic waves. The electrons do cylindrical solenoidal motion with a constant pitch. P_R reaches the peak of the whole process, and radiate electromagnetic waves outward with constant power $P_{R\max}$. The magnetic field is in competition with the laser field. Since the magnetic field prevails in the competition and all the final high-power radiation originates from the magnetic field, we attribute the radiation pattern in the CDM region to the magnetic field radiation.

B. Spatial Radiation Properties of NTFS

To investigate the spatial radiation properties of NTFS, we studied the full angular distribution of the radiated power in the angular plane. Firstly, for each unit solid angle, we calculated the radiated power at each time point during the NTFS. We define the maximum of these as the radiated power P_Ω for that solid angle. It is important to note that P_Ω for different solid angles are obtained at different moments. And the maximum of P_Ω for all solid angles is the maximum radiated power $P_{\Omega\max}$, and we define that solid angle (θ_p, ϕ_p). $P_{\Omega\max} = P_{R\max}$, but the former reflects the spatial properties of the radiation while the latter reflects the temporal properties of the radiation. Taking the azimuthal angle $\phi = \phi_p$, defined on the main peak of radiation, the polar angle difference between the two half-maximum radiated power points $P_{\Omega\max}/2$ is the collimation angle $\Delta\theta$. In this paper, we evaluate the merits of the radiation properties of NTFS from three aspects, namely $P_{\Omega\max}$, θ_p and $\Delta\theta$, which correspond to the intensity, directionality and collimation of the radiation.

In Fig. 4, the spatial properties of the electron radiated power show three typical angular distributions: the radiation in the CDM region is concentrated in a ring with a very small radius and ring width, and the electrons radiate ultrahigh-power electromagnetic waves outward with excellent directionality and
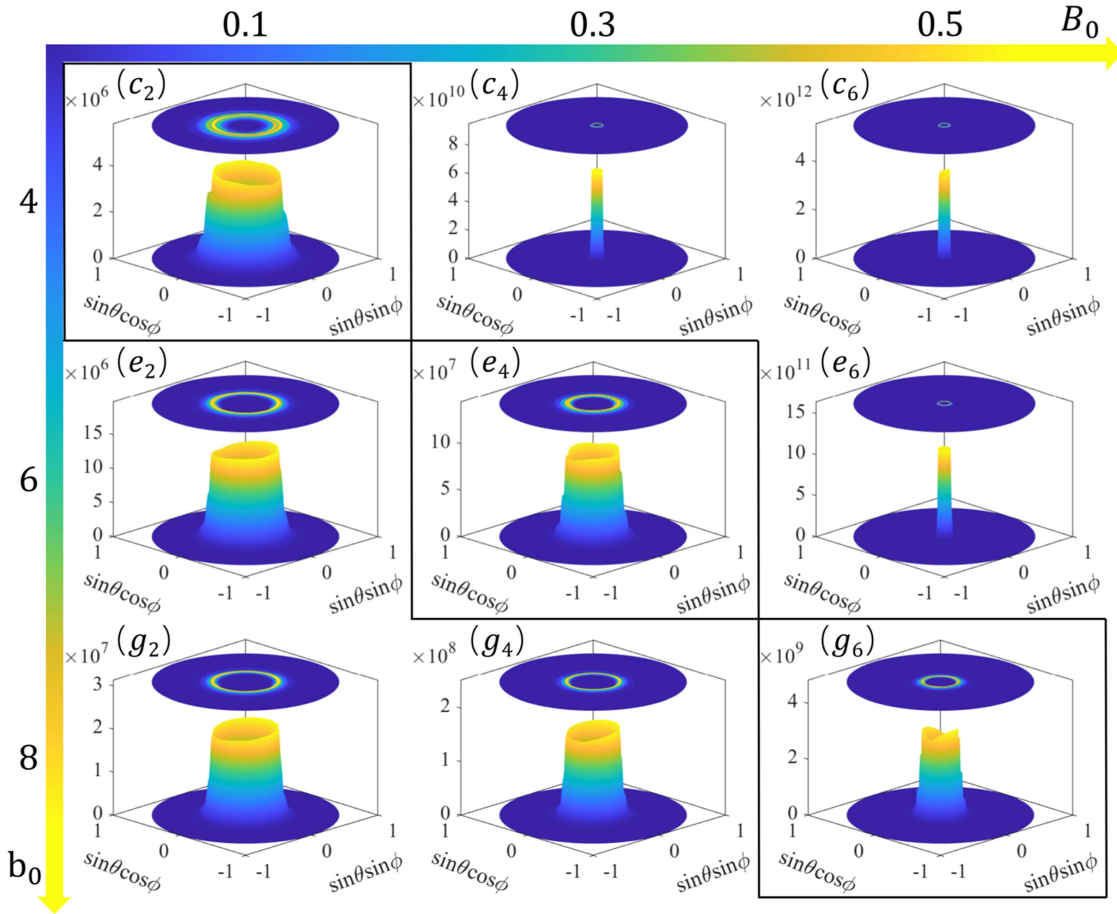
Fig. 4. Full-angle distribution of electron maximum radiated power, where the color scale of each plot is individually normalized by its own peak radiated power. Figure matrix compares different magnetic flux densities B_0 horizontally and beam waist radius b_0 vertically. The black curves in the figure divide the radiation patterns of the NTFS, i.e., the different regions of the superimposed field (see Visualization 2).

high collimation. This is because when the radiation pattern is magnetic field radiation, as shown in Fig. 2, the motion of the electron at the peak radiated power is essentially stable, with $\Delta\theta \to 0$. The denominator term $(1 - \boldsymbol{n} \cdot \boldsymbol{u})^6$ of (5) indicates that the maximum radiated power is approximated to be in the direction of tangent to the velocity. Thus when $u_z \gg u_\perp$, $\boldsymbol{u}$ is approximately parallel to the $+z$ axis and θ is small.

As the beam waist radius increases and gradually transitions to the CDLM region, the ring width of the radiation angle distribution increases significantly, with obvious ripples observed. Taking Fig. 4 (f_6) as an example, arbitrarily selecting a θ, it can be found that P_Ω is continuous and basically constant in size on ϕ. Arbitrarily selecting a ϕ and increasing from $\theta = 0$ to $\theta = \pi$, P_Ω first rises rapidly from a very small value to $P_{\Omega\max}$, and then decays to 0 in a step-like manner across several plateau regions.

The spatial properties of the corrugation phenomenon can be approximated as a multistage ring ladder comprising multiple rings with the same center, where the radius is inversely proportional to the height. At the same time, it is worth emphasizing that for any $B_0 \neq 0$, the ripple phenomenon always exists. And the larger the B_0, the larger the b_0 at which the phenomenon occurs, which is because ripple radiation only occurs when the

intensity of the laser field and the applied magnetic field are matched. When $B_0 = 0$, we find that there will be a transition state between $b_0 = 3 \sim 4$ with radiation space properties similar to ripples, allowing vortex radiation to smoothly transition to cylindrical radiation. Therefore, we include Fig. 4 $(b_1),(c_1)$ into the black ladder as the transition state in the magnetic field-free region.

Further increase the beam waist radius to enter the CDL region. Compared with the CDM region, although both regions have a hollow cylindrical angular distribution of radiation, the radiated power, directionality and collimation of the CDL region are far worse. This is because when the radiation pattern is laser field radiation, the energy of electrons is much smaller than magnetic field radiation, so $\theta_{CDL} > \theta_{CDM}$ can be obtained from $\theta \propto 1/\gamma$. At the same time, during the process of radiating peak power in the CDL region, electrons move relatively from the rising edge to the falling edge of the laser, with constant changes in motion state, resulting in poor collimation.

C. Ripple Phenomenon

We define the brightest main peak of radiation in the center on the angular plane as the core ripple, while rings of
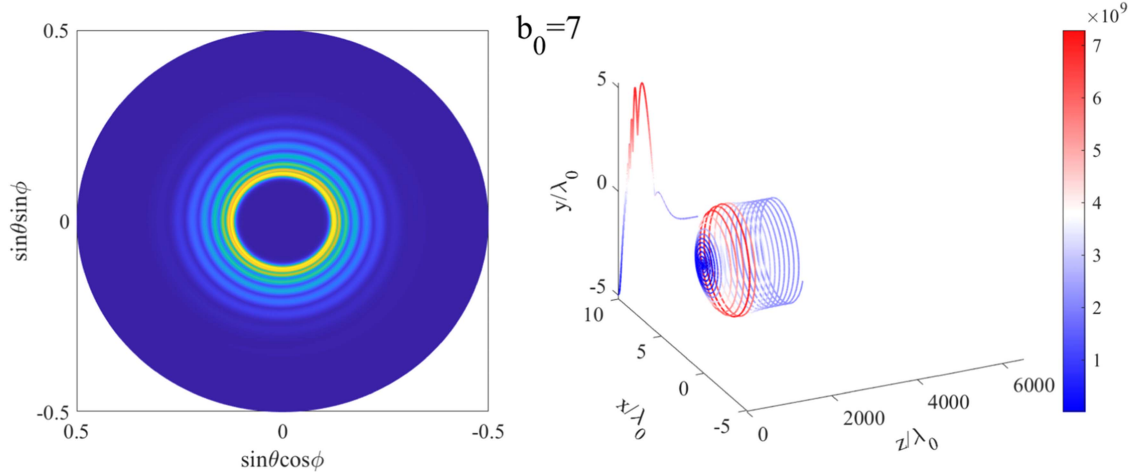
Fig. 5. On the left is a projection of the full angular distribution of the maximum radiated power of electrons in the cylindrical coordinate system. To highlight the regions with significant radiation, only the angular plane of $\theta \in [0°, 30°]$ is shown on the plot. On the right are the electron trajectory and radiated power curves. The magnetic flux density $B_0 = 0.5$, the beam waist radius b_0 is labeled in the center. The color scale of each frame is normalized by the peak radiated power of that frame (see Visualization 3).

radiation with less power on its periphery are defined as the outer ripples, and the inner one as the inner ripples. In Fig. 5 when $b_0 \leq 6$, the radiation in the angular plane is concentrated on the thin and narrow core ripple, and a small number of ripples diverge from the core ripple and slowly diffuse outward into the outer ripples. From the colorbar, it can be found that $P_{R\max}$ is essentially unchanged, and the radiation pattern is still dominated by magnetic field radiation at this time.

Continuing to increase b_0, $P_{R\max}$ cliff attenuates by three orders of magnitude, and the radiation pattern transitions from magnetic field radiation to ripple radiation. The core ripple spreads out in the direction where θ becomes larger, while a circle of outer ripples surfaces successively from the inside out, gradually becoming clearer. The $r_{\perp\max}$ and d_{zmax} of the electrons decrease dramatically, and the trajectory segment where radiates $P_{R\max}$ gradually translates forward from the end of the trajectory to the front of $r_{\perp\max}$. The ripple phenomenon is most obvious when $b_0 = 7$. The outer ripples are gradually lit up from the inside out, and the spatial range covered by the high-power radiation reaches its widest. At the same time, the core ripple is no longer the innermost ring ripple, but is slowly shifted outward and its angular domain is replaced by the inner ripples. Then the outermost ripples no longer spread outward, while the inner ripples expand outward and keep fusing the ripples on the path. At this time, it can be clearly observed that $r_\perp$ at the end of the electron trajectory is significantly smaller than $r_{\perp\max}$. And P_R at the end of the radiation curve is also decreasing, which indicates that the electron starts to experience a deceleration period.

When $b_0 = 8.25$, $P_{R\max}$ stops decaying and starts to grow slightly. The $r_\perp$ at the end of the trajectory and the P_R at the end of the radiation curve are essentially 0. The full angular distribution of the radiation returns to ring once again, which indicates that the radiation pattern has been transformed into laser field radiation.

Ripple radiation, as a transitional radiation pattern, completes the shift from magnetic field radiation to laser field radiation by diffusing and then fusing the ripples from the inside out. The spatial distribution of radiation is transformed from a small ring of ultra-high power to a large ring of low power. Based on the step-like radiation properties of the ripple phenomenon, the radiated power can be obtained by adjusting θ at different levels. If $\theta \& \phi$ are adjusted simultaneously, radiated power of any magnitude from 0 to $P_{\Omega\max}$ can be obtained. The most important thing is that the above operation requires much less angular accuracy of the detector than the usual ring radiation.

Based on the special spatial structure of ripple radiation, there are potential practical applications in many fields. In the biomedical field, the structure allows precise adjustment of the radiation intensity for X-rays and γ-rays during the imaging process, enabling hierarchical imaging and enhanced imaging details. In addition, it is well suited for targeted radiation therapy, such as Gamma Knife. In the field of laser detection, the fine adjustment of power can better meet the requirements of non-destructive testing of cultural artifacts. At the same time, the stepped modulation properties enable flexible adjustment of radiation intensity in remote sensing applications, thus obtaining the best detection effect under different environmental conditions. This is particularly important for atmospheric monitoring, climate change research and other fields.

The evolution of the stages of the electron trajectories radiating $P_{R\max}$ leads to the evolution of the radiation pattern. The $P_{R\max}$ of the magnetic field radiation appears at the end of the trajectory. While the $P_{R\max}$ of the laser field radiation appears in the middle section of the trajectory when b_0 is larger. When transitioning from the CDL region to the CDM region, the peak radiation point gradually shifts from the falling edge of the Gaussian pulse to the junction of the rising and falling edges of the Gaussian pulse. Understood in conjunction with (5), the mechanism for radiating $P_{R\max}$ changes from relying on no small acceleration based on a large velocity to a very
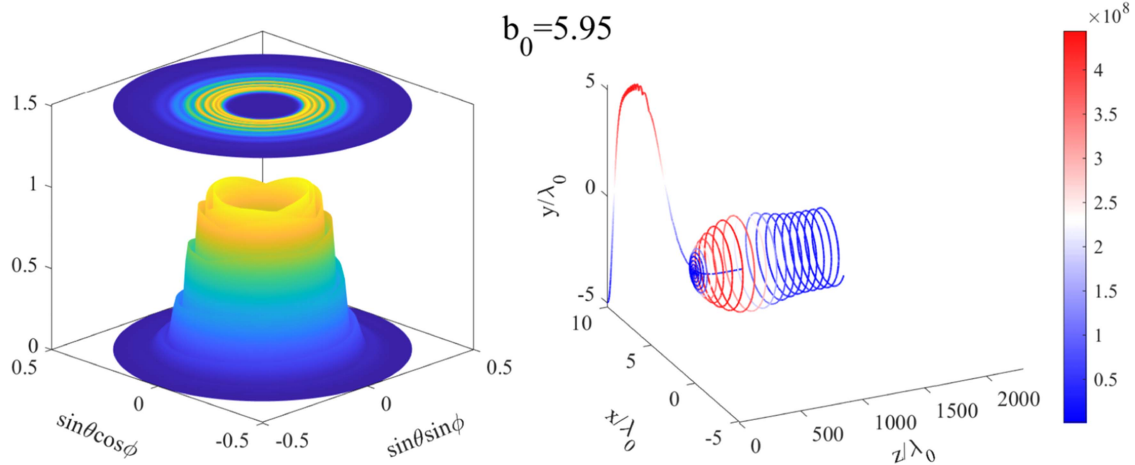
Fig. 6. On the left is the full angular distribution of the maximum radiated power of electrons in the cylindrical coordinate system. To highlight the regions with significant radiation, only the angular plane of $\theta \in [0°, 30°]$ is shown on the plot. On the right are the electron trajectory and radiated power curves. The magnetic flux density $B_0 = 0.5$, the beam waist radius b_0 is labeled in the center. The color scale of each frame is normalized by the peak radiated power of that frame (see Visualization 4).

large velocity supplemented by a very small acceleration. At this point, a slight change in velocity will result in a large change in P_R, so the high-power radiation lasts for a very short time.

As a transitional state, ripple radiation has $P_{R\,\text{max}}$ appearing in a trajectory segment where the orbiting radius $r_\perp$ continues to increase. At this time, P_M is slightly larger than $P_L + P_R$, and the acceleration of the magnetic field is symmetrically offset by the deceleration of the laser field. The ripple phenomenon can be seen as the interface between the two. So the changes in velocity and acceleration are slow and small, and the high-power radiation will last for more optical circles, corresponding to a circle of ripples in the spatial distribution. The larger $\Delta r_\perp$ between the red optical circles corresponds to the θ range covered by the ripple radiation.

D. Lotus Phenomenon

The lotus phenomenon is a special spatial property obtained by the superposition of the ripple radiation on θ with the high-frequency oscillation of the radiated power on ϕ, which better reflects the competitive relationship between the laser field and the applied magnetic field. In Fig. 6, the evolution of the spatial distribution of radiation at the initial time is exactly the same as the ripple phenomenon. Due to the attenuation of $P_{\Omega\,\text{max}}$ at the core ripple, the normalized outer ripple climbs upward, and the overall spatial distribution of the radiation shows a stepped ring shape. When $b_0 = 5.9$, the core ripple and the inner and outer ripple on its edge begin to differentiate into petal-shaped radiation peaks on ϕ. This corresponds to the intensive high-frequency small-amplitude oscillations in the $P_{R\,\text{max}}$ segment of the radiation curve, which is the essential cause of the lotus phenomenon.

On the one hand, we start from the deceleration of the laser field. The radial factor of the laser field is neglected in the CDLM region since $r_{\perp\,\text{max}} \ll b_0$. Considering again the longitudinal Gaussian distribution of the laser, it can be analyzed that $|P_L|$ should increase first and then decrease according

to $|P_L| \propto |\partial a_l / \partial \eta|$. On the other hand, consider the acceleration effect of the applied magnetic field. Since the current trajectory segment radiates $P_{R\,\text{max}}$, $\Delta P_E \approx 0$ and thus $W_{Mz} \approx 0$ and $\Delta u_z \approx 0$. Therefore, we only need to consider $P_{M\perp} \propto r_\perp$ provided by the applied magnetic field. According to $r_\perp$ in the trajectory diagram on the right side of Fig. 6, $P_{M\perp}$ should be increasing and then decreasing before stabilizing. In the process of ripple radiation, if the laser field parameters and magnetic field parameters are selected appropriately, it will lead to a very similar, or even almost the same, change process of $|P_L|$ and $P_{M\perp}$. At this time, in the trajectory segment where radiates $P_{R\,\text{max}}$, the position of the dominant force continuously changes between the two at high frequency, causing the longitudinal acceleration of electrons to swing frequently between positive and negative. This gives rise to high-frequency oscillations of the electron radiation, resulting in the lotus phenomenon.

In addition, we discovered for the first time that NTFS has quasi-periodicity in the azimuth angle ϕ with respect to the beam waist radius b_0. Thanks to the structure of the radiation peaks of the lotus phenomenon, we can clearly observe the non-uniform periodic rotation of the petals of the lotus on ϕ.

E. Full-Angle Distribution of NTFS Temporal Intensity

Fig. 7 is the θ-angle distribution of NTFS pulses per unit time at the ϕ_p angle. Each of its radiation peaks represents one revolution of the electron trajectory around the circle. Define the total span of radiation peaks on θ in each plot as θ_{BW}. And the difference of θ angle between two points half of the maximum value of each radiation peak is $\Delta\theta_{FWHM}$, which can also be used as a criterion for radiometric collimation.

In the CDM region, since electrons perform a stable relativistic spiral motion approximately at the speed of light, the three-dimensional temporal spectrum is a femtosecond pulse array, showing excellent directionality and collimation. Connecting the peak points of the pulse array, it is found that it is consistent with the radiated power curves in Fig. 2. The radiated power in
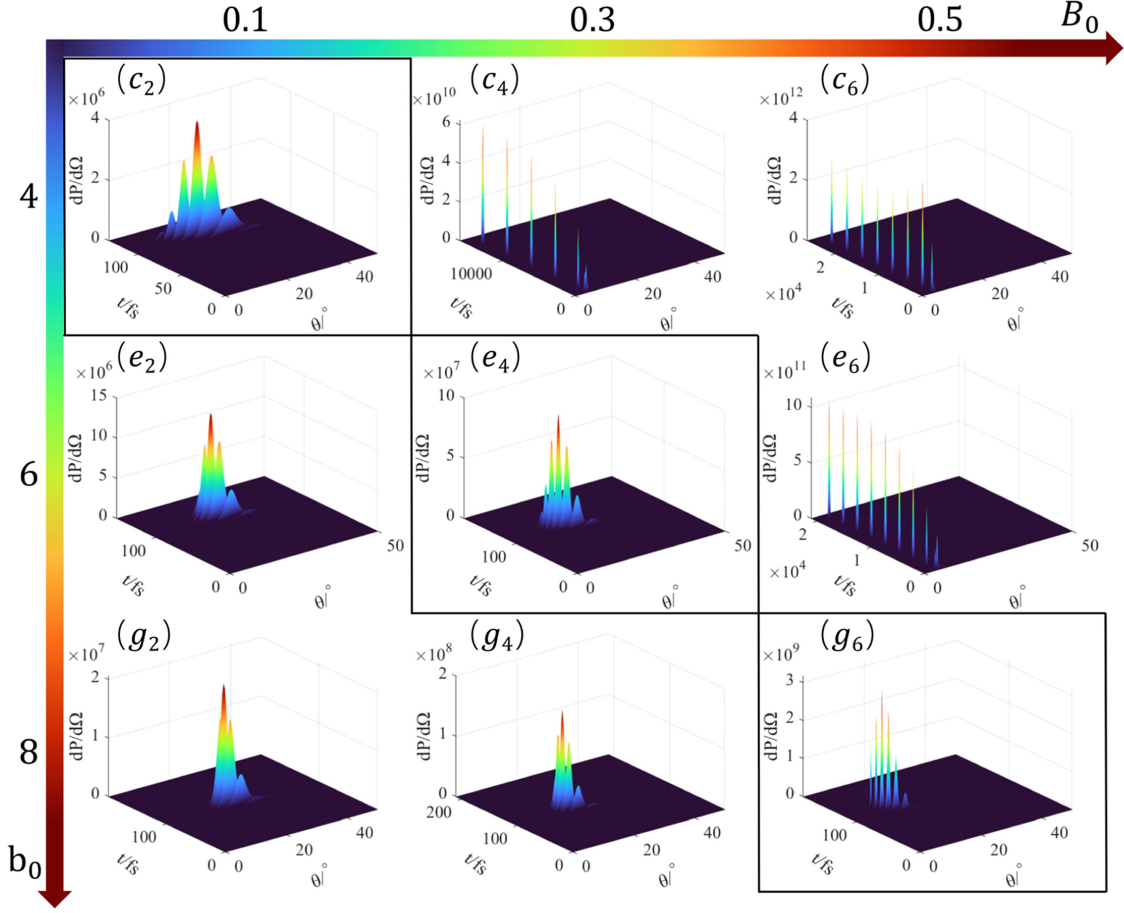
Fig. 7. The joint distribution of the NTFS in time and polar angle θ for an observation angle of (θ, ϕ_p), with each plot separately normalized by its own maximum. Figure matrix compares different magnetic flux densities B_0 horizontally, and different beam waist radius b_0 vertically. The black curves in the figure divide the radiation patterns of the NTFS, i.e., the different regions of the superimposed field (see Visualization 5).

the CDM region is three orders of magnitude higher than in the other two regions.

And when transitioning to the CDLM region, Fig. 7 $(f6)$ clearly demonstrates both the laser field radiation and the magnetic field radiation. The time span between the radiation peaks of magnetic field radiation is large, and they are distributed at small polar angles with extremely small θ_{BW}. The time scale of the laser field radiation is reduced by two orders of magnitude, and the radiation peaks are gathered together to form a pulse group. Each radiation peak in Fig. 7 $(d4)$ corresponds to a ring of ripple in Fig. 4 $(d4)$. The θ_{BW} of the pulse group corresponds to the radius difference between the outer ripples and inner ripples in the full angular distribution of ripple radiation.

Unlike the vortex radiation [29] in Fig. 7 $(a1)$, the directional transformation of the spatial distribution is accomplished with three radiation peaks through the larger $\Delta\theta_{FWHM}$ of each radiation peak. While the $\Delta\theta_{FWHM}$ of the ripple radiation is only slightly larger than that in the CDL region, which mainly realizes the large θ_{BW} by increasing the number of radiation peaks. As time increases, the angle between the radiation peak and the θ axis (i.e., the x-axis) becomes larger and larger, from parallel at the beginning to nearly perpendicular later. The two influencing factors, the orbiting radius $r_\perp$ and the electron radial velocity $u_\perp$, change synchronously. It is just that the influence of $r_\perp$ dominates before the appearance of the main peak, while $u_\perp$ dominates after the main peak.

In the CDL region, as the beam waist radius b_0 increases, θ_{BW} shrinks gradually and is much smaller than that in the CDLM region. The angular distribution of θ is different from that in the CDM region where the radiation peaks are on a straight line, or in the CDLM region where the radiation peaks are symmetric with the main radiation peak as the symmetry axis. The θ of the main radiation peak in the CDL region is smaller than all the secondary peaks, and so is the $\Delta\theta_{FWHM}$. And the pulse group is axisymmetric on the time scale with the main radiation peak as the symmetry axis, indicating the symmetric work process of the laser's rising and falling edges.

F. Coupling Effects of Magnetic Flux Density and Beam Waist Radius on the NTFS

In this section, we investigate the coupling effect of the magnetic flux density and the beam waist radius on NTFS. Although the red and black lines in Fig. 8(a), (b), and (d) are marked independently according to their respective radiation properties, we find that the lines of the same color in each figure
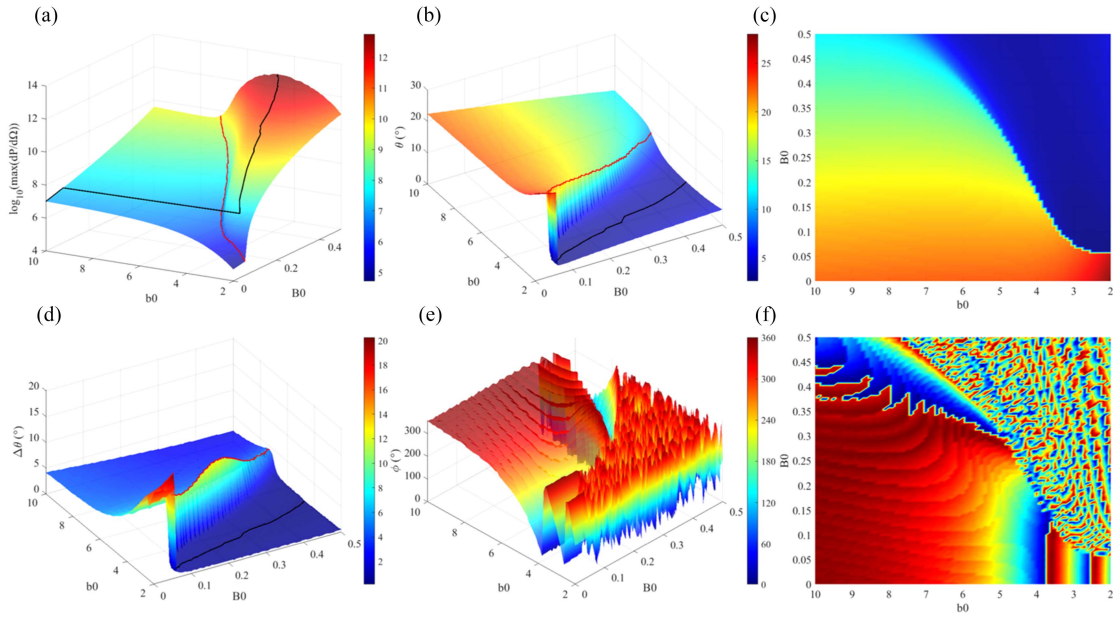
Fig. 8. Under different magnetic flux density B_0 and different beam waist radius b_0, the maximum radiated power of NTFS $\log_{10}(dP_{\Omega\max}/d\Omega)$ (a), the polar angle θ_p where $P_{\Omega\max}$ is located (b) and its projection (c), the collimation angle $\Delta\theta$ of the main radiation peak (d), the azimuth angle ϕ_p where $P_{\Omega\max}$ is located (e) and its projection (f). The red line is the dividing line for the mutation of $\log_{10}(dP_{\Omega\max}/d\Omega)$ (a), the dividing line for the mutation of θ_p (b), and the maximum value of $\Delta\theta$ at each magnetic flux density B_0 (d). The black line is the maximum value of $\log_{10}(dP_{\Omega\max}/d\Omega)$ (a), the minimum value of θ_p (b), and the minimum value of $\Delta\theta$ (d) at each magnetic flux density B_0.

overlap nearly exactly. For the black line this indicates that for any magnetic flux density B_0, there is always a beam waist radius b_0 such that all three aspects of the radiation properties are simultaneously optimized. The red line corresponds to the parameter where the ripple phenomenon is most obvious and is the dividing line between the CDL region (laser field radiation) and the CDM region (magnetic field radiation), where a jump in the radiation properties is experienced. Examining the envelope and trend of the three plots as a whole again, (b) and (d) are both in perfect agreement and perfectly complementary to (a). This suggests that the superiority or inferiority of the various aspects of the radiation properties is completely bound as the parameters are varied. Thus, we can choose the parameter combination based on which all the radiation properties of NTFS are optimal at the same time, i.e., $B_0 = 0.5$, $b_0 = 4.7$. At this time, $P_{\Omega\max} = 5.685 \times 10^{12}$ (which is normalized by $e^2\omega_0^2/4\pi c$), $\theta_p = 3.375°$ and $\Delta\theta = 0.125°$. $P_{\Omega\max}$ reaches the maximum, while θ_p and $\Delta\theta$ reach the minimum, which is a very ideal radiation source [33].

Fig. 8(a) is instructive for the selection of field parameters based on modulation power. The black line shows a jump point at $B_0 = 0.85$, indicating that the $P_{\Omega\max}$ of the laser field radiation is higher than that of the magnetic field radiation when the B_0 is small, and the largest possible b_0 should be selected at this time. As for the magnetic field radiation, the distribution of $P_{\Omega\max}$ is approximately symmetric about the black line. At this time, a moderate size of b_0 should be chosen to deepen the cooperation of the superimposed field at the rising edge and weaken the competition at the falling edge, so that the electrons can obtain as much energy as possible. It is also important to emphasize that $P_{\Omega\max}$ is still vertically increasing by several orders of

magnitude at the red line, even when the z-axis coordinate is logarithmic. This indicates the seminal importance of magnetic field radiation for modulating ultra-high-power radiation.

Fig. 8(b) and (c) explore the effect of the crossover parameter on the directionality of $P_{\Omega\max}$. The projection plot clearly shows that θ_p is generally small in the CDM region, much smaller than that in the CDL region. For magnetic field radiation, the parameter has a negligible effect on its collimation. However, for laser field radiation, increasing B_0 can significantly reduce θ_p. Interestingly, the red line in Fig. 8(d) is like a ridge. This indicates that the $\Delta\theta$ at ripple radiation is much larger than the other radiation patterns, which is related to its step-like spatial distribution. When $B_0 = 2.6$, a secondary peak appears in $\Delta\theta$, indicating that the radius difference between the inner and outer ripples on the angular plane reaches the maximum at this time. As the steps widen, the accuracy requirements for the detector are further reduced.

Comparing the two projections Fig. 8(c) and (f), it is found that the joint distribution of ϕ_p with respect to B_0 and b_0 is divided in two by the ripple phenomenon as in the case of the radiation properties. In the CDM region, $P_{\Omega\max}$ can be observed at different azimuthal angles ϕ because the radiating $P_{\Omega\max}$ is the red trajectory segment in Fig. 2 that does a steady winding with constant pitch and $r_\perp$. So ϕ_p is a random number between $[0°, 360°]$, which corresponds to the jagged and irregular distribution of ϕ_p in the region in Fig. 8(e). And in the CDL region, we discovered for the first time that NTFS has quasi-periodicity in the azimuth angle ϕ with respect to the beam waist radius b_0, which is contrary to the common understanding of previous researchers. As shown in Fig. 8(e), for any magnetic flux density, ϕ_p varies continuously and periodically as b_0 increases, and the

rate of change is negatively correlated with b_0. Since $\varphi_0 = 0$ in this paper, (2) can be simplified to $\varphi = \eta + \varphi_R - \varphi_G$. And again, since $R(z) \gg \rho^2$ leads to φ_R being a very small quantity, $\varphi \approx \eta - \varphi_G$. On the one hand, whether it is laser field radiation or magnetic field radiation, the phase factor η when radiating $P_{R\max}$ is always close to $\eta = 0$ with the increase of b_0, which is the junction of the rising and falling edge of the laser. And the closer η is to $\eta = 0$ the smaller is the magnitude of its change. On the other hand, according to the abscissa of the trajectory in Fig. 2, it is not difficult to find that the smaller b_0 is, the more orders of magnitude z/z_f will change when the unit b_0 is changed, which will further affect the change rate of φ_G. It is worth noting that since $\varphi_G \in (0, \pi/2)$ and the slope is large when z/z_f is close to 0, the effect of η on φ dominates when b_0 is small, while φ_G dominates when b_0 is large.

Unlike the beam waist radius b_0, the magnetic flux density B_0 has little effect on ϕ_p. Taking $b_0 = 10$ in Fig. 8(e) as an example, we can find that ϕ_p for different B_0 is a wavy line with tiny undulations. However, it can still be found that this effect is greater the larger B_0 is by the height of the wave undulations. Meanwhile, according to a wave parallel to each other and perpendicular to the B_0 axis in the figure, it can be concluded that the influence of B_0 on ϕ_p is relatively constant with respect to b_0.

IV. CONCLUSION

In conclusion, based on Big Data, we studied in detail the nonlinear Thomson forward scattering of relativistic electrons in a circularly polarized laser field with an applied magnetic field from the perspectives of spatial distribution and time distribution. The coupling effect of magnetic flux density and beam waist radius on electron trajectories, spatial distribution and temporal structure of radiation are specifically investigated. Based on the joint distribution of this pair of cross parameters, we classify three types of radiation patterns according to the spatiotemporal properties of radiation. That is, magnetic field radiation, ripple radiation and laser field radiation, which correspond to the three partitions CDM, CDLM, and CDL, respectively. We probe deeply into the process of radiation pattern evolution from the perspective of electron trajectories, the spatial and temporal spectrum of radiation. And we explain the mechanism of radiation pattern evolution by the competition and cooperation between laser and magnetic fields from the field intensity relation of the superimposed field. We find that ripple radiation structures and lotus phenomena appear when the forces of two fields are matched. This unique spatial distribution not only serves as an intuitive basis for judging the switching of radiation patterns, but also significantly reduces the precision requirements of the detector during actual detection, which is more in line with the current laboratory conditions. It also realizes the modulation of stepped radiated power or arbitrary radiated power. In addition, we find that the radiation properties of the magnetic field radiation are much better than those of the laser field radiation, especially the maximum radiated power can be increased by at least three orders of magnitude. A highly collimated NTFS with the highest maximum radiated power and

the best directionality can be obtained when the magnetic flux density $B_0 = 0.5$ and the beam waist radius $b_0 = 4.7$. This provides a brand new modulation pathway for the laboratory modulation of super intense X/γ rays. Interestingly, we break the previous knowledge that the phase angle ϕ_p at maximum radiated power has randomness by using Big Data. We find that ϕ_p has a quasi-periodicity about b_0, but is largely independent of B_0.

REFERENCES

[1] K. Lee, Y. Cha, M. Shin, B. Kim, and D. Kim, "Temporal and spatial characterization of harmonics structures of relativistic nonlinear Thomson scattering," *Opt. Exp.*, vol. 11, no. 4, pp. 309–316, Feb. 2003, doi: 10.1364/OE.11.000309.

[2] R. Bartels et al., "Shaped-pulse optimization of coherent emission of high-harmonic soft X-rays," *Nature*, vol. 406, no. 6792, pp. 164–166, Jul. 2000, doi: 10.1038/35018029.

[3] D. E. Spence, P. N. Kean, and W. Sibbett, "60-fsec pulse generation from a self-mode-locked Ti:Sapphire laser," *Opt. Lett.*, vol. 16, no. 1, pp. 42–44, Jan. 1991, doi: 10.1364/OL.16.000042.

[4] M. Leonetti, C. Conti, and C. Lopez, "The mode-locking transition of random lasers," *Nature Photon.*, vol. 5, no. 10, pp. 615–617, Oct. 2011, doi: 10.1038/nphoton.2011.217.

[5] Y. Jeong, J. K. Sahu, D. N. Payne, and J. Nilsson, "Ytterbium-doped large-core fiber laser with 1.36 kW continuous-wave output power," *Opt. Exp.*, vol. 12, pp. 6088–6092, 2004.

[6] Z. T. Wang, Y. Chen, C. J. Zhao, H. Zhang, and S. C. Wen, "Switchable dual-wavelength synchronously Q-switched erbium-doped fiber laser based on graphene saturable absorber," *IEEE Photon. J.*, vol. 4, no. 3, pp. 869–876, Jun. 2012, doi: 10.1109/JPHOT.2012.2199102.

[7] M. Pessot, D. J. Harter, J. Squier, and G. Mourou, "Chirped-pulse amplification of 100-fsec pulses," *Opt. Lett.*, vol. 14, no. 15, pp. 797–799, Aug. 1989, doi: 10.1364/OL.14.000797.

[8] P. Maine, D. Strickland, P. Bado, M. Pessot, and G. Mourou, "Generation of ultrahigh peak power pulses by chirped pulse amplification," *IEEE J. Quantum Electron.*, vol. 24, no. 2, pp. 398–403, Feb. 1988, doi: 10.1109/3.137.

[9] A. Dubietis, R. Butkus, and A. P. Piskarskas, "Trends in chirped pulse optical parametric amplification," *IEEE J. Sel. Topics Quantum Electron.*, vol. 12, no. 2, pp. 163–172, Mar./Apr. 2006, doi: 10.1109/JSTQE.2006.871962.

[10] U. Keller, "Recent developments in compact ultrafast lasers," *Nature*, vol. 424, no. 6950, pp. 831–838, Aug. 2003, doi: 10.1038/nature01938.

[11] Y. Qingyu, W. Yubo, and T. Youwei, "Ultrashort and high-collimation X/γ-rays generated by nonlinear inverse Thomson scattering between off-axis electrons and circularly polarized intense laser pulses," *Opt. Exp.*, vol. 31, no. 17, Aug. 2023, Art. no. 27723, doi: 10.1364/OE.494538.

[12] S. H. Glenzer and R. Redmer, "X-ray Thomson scattering in high energy density plasmas," *Rev. Modern Phys.*, vol. 81, no. 4, pp. 1625–1663, Dec. 2009, doi: 10.1103/RevModPhys.81.1625.

[13] G. Sarri et al., "Ultrahigh brilliance Multi-MeV γ-ray beams from nonlinear relativistic Thomson scattering," *Phys. Rev. Lett.*, vol. 113, no. 22, Nov. 2014, Art. no. 224801, doi: 10.1103/PhysRevLett.113.224801.

[14] C. K. Hagen et al., "Low-dose X-ray phase contrast tomography: Experimental setup, image reconstruction and applications in biomedicine," in *Proc. IEEE Nucl. Sci. Symp. Med. Imag. Conf.*, 2014, pp. 1–5, doi: 10.1109/NSSMIC.2014.7430971.

[15] G. Harding and B. Schreiber, "Coherent X-ray scatter imaging and its applications in biomedical science and industry," *Radiat. Phys. Chem.*, vol. 56, no. 1/2, pp. 229–245, Aug. 1999, doi: 10.1016/S0969-806X(99)00283-2.

[16] J. Crawford et al., "Towards quantum telescopes: Demonstration of a two-photon interferometer for precision astrometry," *Opt. Exp.*, vol. 31, no. 26, pp. 44246–44258, Dec. 2023, doi: 10.1364/OE.486342.

[17] C. Cai et al., "Search for gamma-ray bursts and gravitational wave electromagnetic counterparts with high energy X-ray telescope of insight-HXMT," *Monthly Notices Roy. Astronomical Soc.*, vol. 508, no. 3, pp. 3910–3920, Oct. 2021, doi: 10.1093/mnras/stab2760.

[18] M. Sato et al., "Assessment of multi-pulse laser-induced damage threshold of metallic mirrors for Thomson scattering system," *Opt. Exp.*, vol. 21, no. 8, pp. 9333–9342, Apr. 2013, doi: 10.1364/OE.21.009333.

[19] J. Kostamovaara et al., "On laser ranging based on high-speed/energy laser diode pulses and single-photon detection techniques," *IEEE Photon. J.*, vol. 7, no. 2, Apr. 2015, Art. no. 7800215, doi: 10.1109/JPHOT.2015.2402129.

[20] X. Zhang, D. Chen, and Y. Tian, "Analysis of the pulse widths on radiation properties from an electron driven by intense elliptically polarized laser," *Appl. Phys. B*, vol. 129, no. 8, Aug. 2023, Art. no. 135, doi: 10.1007/s00340-023-08066-z.

[21] Y. Yan, X. Zhou, and Y. Tian, "Influence of high-energy electron's initial position on its spatial radiation characteristics during interaction with a linearly polarized tightly focused laser," *Opt. Quantum Electron.*, vol. 54, no. 12, Dec. 2022, Art. no. 865, doi: 10.1007/s11082-022-04162-0.

[22] L. Zhao, Z.-J. Chen, H.-B. Sang, and B.-S. Xie, "Spatial characteristics of Thomson scattering spectra in laser and magnetic fields∗," *Chin. Phys. Lett.*, vol. 36, no. 7, Jul. 2019, Art. no. 074101, doi: 10.1088/0256-307X/36/7/074101.

[23] F. H. M. Faisal and Y. I. Salamin, "Electron dynamics and photon-emission spectra in an ultrashort laser pulse and a uniform magnetic field," *Phys. Rev. A*, vol. 60, no. 3, pp. 2505–2516, Sep. 1999, doi: 10.1103/PhysRevA.60.2505.

[24] C. Jiang, H. Z. Xie, H. B. Sang, and B. S. Xie, "Thomson backscattering in combined fields with a general elliptical polarization," *Europhysics Lett.*, vol. 117, no. 4, Feb. 2017, Art. no. 44002, doi: 10.1209/0295-5075/117/44002.

[25] X. Hong, D. Wei, Y. Li, R. Tang, J. Sun, and W. Duan, "Enhanced radiation of nonlinear Thomson backscattering by a tightly focused Gaussian laser pulse and an external magnetic field," *Europhysics Lett.*, vol. 139, no. 1, Jul. 2022, Art. no. 14001, doi: 10.1209/0295-5075/ac7c2f.

[26] R. Nishiura and K. Ioka, "Collective Thomson scattering in magnetized electron and positron pair plasma and the application to induced Compton scattering," *Phys. Rev. D*, vol. 109, no. 4, Feb. 2024, Art. no. 043048, doi: 10.1103/physrevd.109.043048.

[27] A. A. Mushtukov, D. I. Nagirner, and J. Poutanen, "Compton scattering S matrix and cross section in strong magnetic field," *Phys. Rev. D*, vol. 93, no. 10, May 2016, Art. no. 105003, doi: 10.1103/PhysRevD.93.105003.

[28] A. A. Mushtukov et al., "Statistical features of multiple Compton scattering in a strong magnetic field," *Phys. Rev. D*, vol. 105, no. 10, May 2022, Art. no. 103027, doi: 10.1103/PhysRevD.105.103027.

[29] Y. Wang, Q. Zhou, J. Zhuang, P. Yu, and Y. Tian, "Vortex and symmetric radiation character of nonlinear Thomson scattering in Laguerre-Gaussian circularly polarized laser pulses," *Opt. Exp.*, vol. 29, no. 14, pp. 22636–22647, Jul. 2021, doi: 10.1364/OE.426529.

[30] F. He et al., "Ponderomotive acceleration of electrons by a tightly focused intense laser beam," *Phys. Rev. E*, vol. 68, no. 4, Oct. 2003, Art. no. 046407, doi: 10.1103/PhysRevE.68.046407.

[31] J. A. Barandes, "On magnetic forces and work," *Found. Phys.*, vol. 51, no. 4, pp. 79–95, Aug. 2021, doi: 10.1007/s10701-021-00483-4.

[32] J. A. Barandes, "Can magnetic forces do work?," 2023, *arXiv:1911.08890*.

[33] Y. Zhang et al., "Optimum beam waist radius under applied magnetic field for optimal radiation properties of nonlinear Thomson scattering," *Appl. Phys. B-Lasers O*, vol. 130, no. 3, Feb. 2024, Art. no. 43, doi: 10.1007/s00340-024-08178-0.